Parameterization of Mixed Layer Eddies. II: Prognosis and Impact

Baylor Fox-Kemper
*Department of Earth, Atmospheric and Planetary Sciences, Massachusetts Institute of Technology, Cambridge, Massachusetts, 01239**

Raffaele Ferrari
Department of Earth, Atmospheric and Planetary Sciences, Massachusetts Institute of Technology, Cambridge, Massachusetts, 01239

(8 October 2007)

ABSTRACT

Fox-Kemper et al. (2007a) propose a parameterization for restratification by mixed layer eddies that develop from baroclinic instabilities of ocean fronts. The parameterization is cast an overturning streamfunction that is proportional to the product of horizontal buoyancy gradient, mixed layer depth, and inertial period. The parameterization has remarkable skill for an extremely wide range of ML depths, rotation rates, vertical and horizontal stratifications. In this paper a coarse resolution prognostic model of the parameterization is compared with submesoscale mixed layer eddy resolving simulations. The parameterization proves accurate in predicting changes to the buoyancy. The climate implications of the proposed parameterization are estimated by applying the restratification scaling to observations: the mixed layer depth is estimated from climatology, and the buoyancy gradients from satellite altimetry. The vertical fluxes are comparable to monthly mean air-sea fluxes in large areas of the ocean and suggest that restratification by mixed layer eddies is a leading order process in the upper ocean. Critical regions for ocean-atmosphere interaction, such as deep, intermediate, and mode water formation sites, are particularly affected.

1. Introduction

Boccaletti et al. (2007) (hereafter BFF) and Fox-Kemper et al. (2007a) (hereafter FFH) study the restratification due to ageostrophic baroclinic instabilities that develop at fronts in the ocean surface mixed layer. BFF and FFH study the restratification once the instabilities have reached finite amplitude, by focusing on a mixed layer (ML) front in a reentrant channel. First, the front geostrophically adjusts (Tandon and Garrett, 1995), and then yields to ageostrophic baroclinic instabilities (Stone, 1972a). FFH propose that the primary effect of these instabilities on the mean flow is to overturn the front, converting horizontal density gradients to vertical gradients.

The baroclinic instabilities that lead to finite-amplitude mixed layer eddies (MLEs) occur on lengthscales near the deformation radius of the ML, which is O(1km) because of the weak stratification in the ML. General circulation models (GCMs) used for climate studies do not resolve these small scales, so the overturning effect of MLEs must be parameterized. Even "eddy-resolving" GCMs with O(10km) grids require parameterization of the still unresolved submesoscale. The buoyancy fluxes needed for the buoyancy budget in a GCM may be spectrally decomposed into three categories, fluxes by resolved large-scale and mesoscale phenomena ($\overline{\overline{\mathbf{u}}}\overline{\overline{b}}$)[1], submesoscale fluxes ($\overline{\overline{\mathbf{u}'b'}}$), and smaller scale turbulent, solar, and diffusive fluxes $\mathcal{F}$. The double overline indicates horizontal averaging onto the grid of the coarse model, and primes denote submesoscale perturbations from the coarsened averages. The momentum fluxes associated with MLEs are weak and inconsequential to the momentum resolved in the GCM, so only MLE buoyancy fluxes will be considered here. The buoyancy equation for the evolving front in the coarse model becomes,

$$\overline{\overline{b}}_t + \nabla \cdot \left[\overline{\overline{\mathbf{u}}}\overline{\overline{b}} + \overline{\overline{\mathbf{u}'b'}}\right] = -\nabla \cdot \mathcal{F}. \quad (1)$$

Where $b = -g\rho/\rho_0$ is the buoyancy, and $\mathbf{u}$ is the

*Present address: Cooperative Institute for Research in the Environmental Sciences (CIRES) and Department of Atmospheric and Oceanic Sciences, University of Colorado at Boulder, Boulder, Colorado 80309

[1]for simplicity, mesoscale features are considered part of the 'resolved' fluxes whether they are actually resolved or represented with a parameterization.

three dimensional velocity. FFH argue that the bulk of the MLE restratification may be written as an overturning streamfunction,

$$\overline{\overline{\mathbf{u}'b'}} \approx \mathbf{\Psi} \times \nabla\overline{\overline{b}}. \tag{2}$$

FFH also provide a scaling and vertical structure for the streamfunction,

$$\mathbf{\Psi} = C_e \frac{H^2 \nabla\overline{\overline{b}}^z \times \hat{\mathbf{z}}}{|f|}\mu(z), \tag{3}$$

$$\mu(z) = \left[1 - \left(\tfrac{2z}{H} + 1\right)^2\right]\left[1 + \tfrac{5}{21}\left(\tfrac{2z}{H} + 1\right)^2\right]. \tag{4}$$

Where f is Coriolis parameter, and H and $\nabla\overline{\overline{b}}^z$ are the ML depth and buoyancy gradient averaged vertically over the ML in the coarse GCM. The efficiency factor C_e is determined to be in the range $0.06 - 0.08$ by fitting to 241 simulations varying in front width and strength, ML depth, initial stratification and velocity, viscosity, presence of diurnal convection, interior stratification, and rotation rate (Fig. 1, reproduced from FFH). The value used for all prognostic simulations here is $C_e = 0.06$, which is the best fit for simulations without diurnal convection.

Since $\nabla\cdot[\nabla\times(\mathbf{\Psi}\overline{\overline{b}})] = 0$, the MLE flux given in (1) can be written as an advection by an eddy-induced velocity $\mathbf{u}^*$,

$$\overline{\overline{b}}_t + \nabla\cdot\left[(\overline{\overline{\mathbf{u}}} + \mathbf{u}^*)\overline{\overline{b}}\right] = -\frac{\partial\mathcal{F}}{\partial z}, \tag{5}$$

$$\mathbf{u}^* \equiv \nabla\times\mathbf{\Psi}. \tag{6}$$

Recall that any mesoscale eddy effects are included in $\overline{\overline{u}}\overline{\overline{b}}$. This form lends itself to easy numerical implementation (Appendix A). The formulae (3) through (6) parameterize the most important effects of MLEs for GCMs.

This paper features two applications of the parameterization. First, a prognostic coarse resolution simulation using the parameterization is compared directly to a submesoscale-resolving simulation (Section 2). Second, the climate impact of MLE restratification is estimated by applying the parameterization to data from satellite observations and climatologies of the upper ocean (Section 3). Section 4 concludes.

2. Prognostic Model Comparison

BFF and FFH study MLE restratification by focusing on a single ML front in a channel, floating over a more stratified ocean interior. The front at time zero may be considered as the edge of a recently strongly vertical mixed ocean patch or a result of straining of a large-scale gradient by a mesoscale field. Depending on details of the initial conditions, the front soon undergoes gravitational slumping or symmetric instabilities. After these initial transients lasting only a few inertial periods, the along-front geostrophic shear goes baroclinically unstable. Restratification begins in earnest as the instabilities reach finite amplitude and slump over the isopycnals. Fig. 2 shows two snapshots of temperature from a typical simulation: just after the appearance of MLEs and later when MLEs have enlarged due to an inverse cascade.

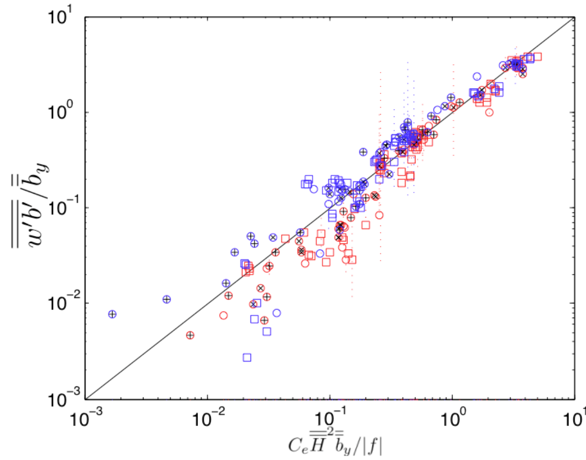

FIGURE 1: Magnitude of diagnosed time average of $\overline{\overline{w'b'}}/\overline{\overline{b}}_y$ from 3d MITgcm submesoscale eddy resolving simulations versus the magnitude of the time average of $C_e\overline{\overline{b}}_y^z H^2/|f|$ with $C_e = 0.08$. A total of 241 simulations are shown varying parameters (with and without diurnal cycle, geostrophically balanced initially or not, varying front width and strength, varying ML depth, varying friction).

FFH propose a parameterization that reproduces the effects of MLEs relevant to models that do not resolve the submesoscale. It consists primarily of an overturning streamfunction that mimics the adiabatic slumping of isopycnals. FFH note that MLEs also drive diabatic buoyancy fluxes, which they refer to as "residual" eddy fluxes, because they are what is left over of $\overline{\overline{\mathbf{u}'b'}}$ beyond the adiabatic fluxes given by $\mathbf{\Psi}\times\nabla\overline{\overline{b}}$. The residual fluxes include an horizontal buoyancy flux that acts to widen the front and a vertical downgradient buoyancy flux at the ML base. In this section a prognostic model that evolves buoyancy according to the parameterization in (3) through (6) is compared directly to a submesoscale resolving simulation. The bulk of MLE restratifi-

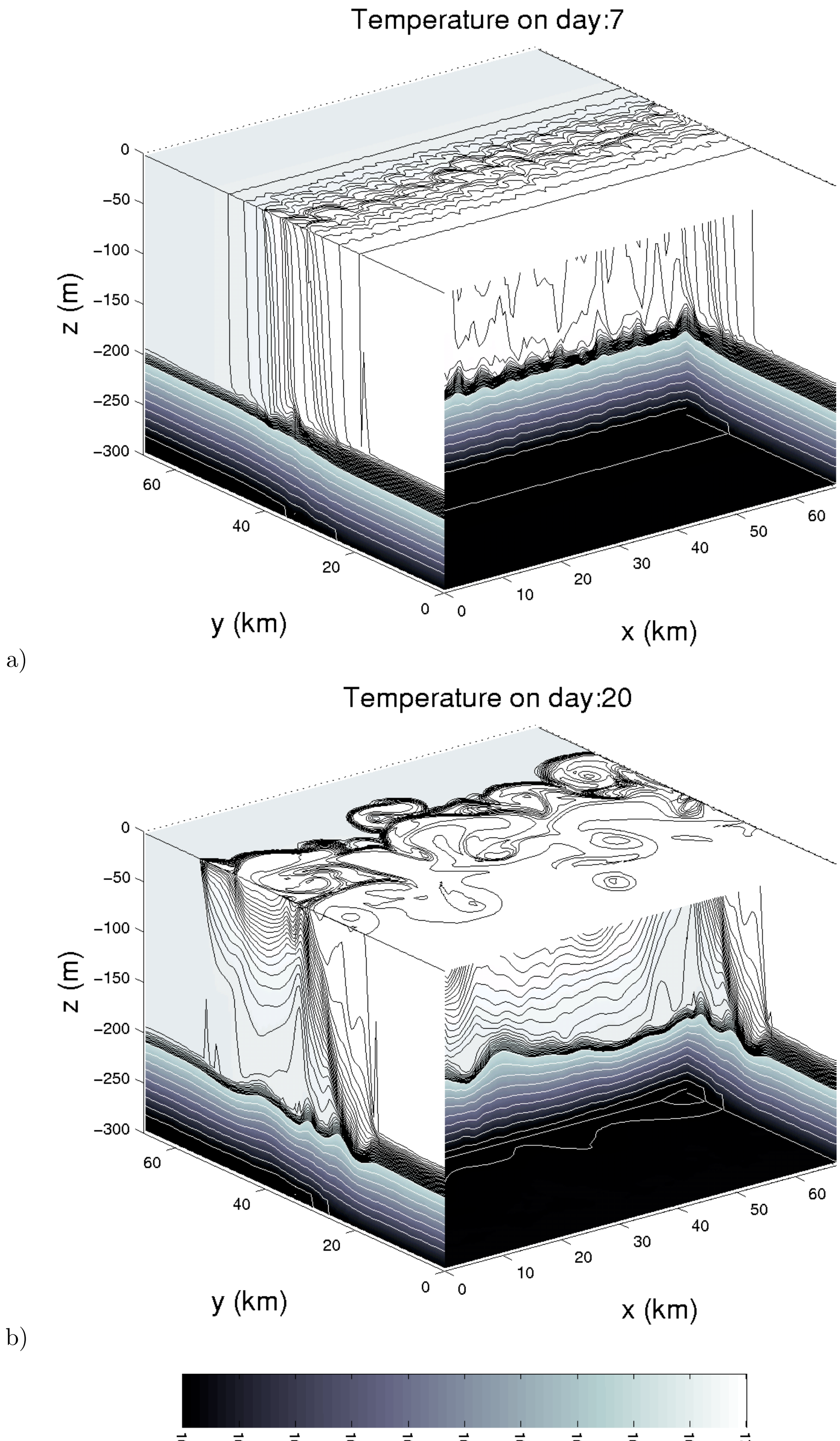

Figure 2: Temperature (^{o}C) during a typical simulations of the adjusting front. (Black contour interval=0.01^{o}C, white contour interval=0.1^{o}C.) Shortly after geostrophic adjustment, the front forms wavelike baroclinic instabilities (upper panel), which enlarge in time and slump the front (lower panel).

Symbol	Name	Value
N_{int}	Interior stratification	$64f$
N_{ml}	ML stratification	0
M^2	front strength	$-(2f)^2$
f	Coriolis parameter	$7.29 \times 10^{-5}\mathrm{s}^{-1}$
L_f	front width	18km
$\Delta x, \Delta y$	horiz. grid	450m
Δz	vert. grid	5m
ν	vert. viscosity	$10^{-4}\mathrm{m}^2/\mathrm{s}$
κ_v	vert. diffusivity	$10^{-5}\mathrm{m}^2/\mathrm{s}$
Sm	Smagorinsky Coeff.	1
κ_h	explicit horiz. diff.	0

Table 1: Constants used in the 3d MITgcm simulation shown here.

cation is shown to be captured by the overturning streamfunction. Including the residual fluxes modifies the solution slightly, but at a significant numerical cost.

A typical 3d simulation (shown in Fig. 2) is chosen from the full set of 241 simulations (shown in Fig. 1) used to validate (3), to be called the 3d model for brevity. The 3d model initial conditions are no initial velocity and a density profile of the form,

$$\overline{\overline{b}} = N^2(z+H) + \frac{L_f M^2}{2} \tanh\left[\frac{2(y-y_o)}{L_f}\right] + b_o, \quad (7)$$

$$N^2 = \begin{cases} N^2_{ml} & \forall : z > -H_o \\ N^2_{int} & \forall : z <= -H_o \end{cases} \quad (8)$$

The basin average of $\overline{\overline{b}}_z$ will be denoted by N^2 below. Parameter values are given in Table 1 and correspond to frontal strengths commonly observed in the ocean–they require only a 0.2°C temperature difference across an 18km front.

The parameterization is implemented in a 2-dimensional model of the $y-z$ plane, to be called the 2d model for brevity. The 2d model solves for the advection of the coarse resolution buoyancy $\overline{\overline{b}}$ by the parameterization streamfunction in (3), using the instantaneous values of $\overline{\overline{b}}$ and H. As this model is only 2d, it cannot develop baroclinic instabilities, so their effect is represented only by the parameterization. The only additional ingredients beyond the equations (3) through (6) are an horizontal boundary condition of $\Psi = 0$ to close the domain, and convective adjustment of buoyancy to eliminate occasional gravitationally unstable profiles caused by discretization errors.[2] Despite its simplicity, the 2d model is fully prognostic and evolves independently given only an initial $\overline{\overline{b}}$ field as input. The numerical details of the 2d model are given in Appendix A.

Symbol	Name	Value
Δy	horiz. grid	9.6km
Δz	vert. grid	5m
κ_v	vert. diffusivity	$10^{-5}\mathrm{m}^2/\mathrm{s}$
κ_h	explicit horiz. diff.	0

Table 2: Constants used in the 2d model of the MLE parameterization.

The 2d model can be initialized with any initial $\overline{\overline{b}}$, but using a snapshot of the buoyancy from the 3d model allows side-by-side comparison of the $\overline{\overline{b}}$ evolution. The parameterization is intended for use in GCMs that will be coarser than the 3d model in both Δx and Δy, so in addition to representing only the along-channel average in x, the 2d model is coarsened in the cross-channel direction y (Table 2). For equal comparison, doubly overlined variables from the 3d model undergo both an along-front average in x *and* an averaging in y to the coarser resolution of the 2d model. The 2d model resolution is in the typical range for "mesoscale eddy resolving" GCMs.

The 2d model is initialized from $\overline{\overline{b}}$ diagnosed from the 3d model on day 7.[3] The two models use the same diffusivity and advection scheme. The 2d model has a larger timestep than the 3d model (although high accuracy is guaranteed by adaptive time-stepping scheme used in the 2d model).

a. *Reproducing the Streamfunction*

A comparison of the frontal spindown in the 2d model and the 3d model (with variables averaged onto the 2d model grid) is shown in Fig. 3. The overturning streamfunction in the 3d model is diagnosed in the Held and Schneider (1999) form, $\Psi_{\mathrm{hs}} = \overline{\overline{w'b'}}/\overline{\overline{b}}_y$: the natural choice here as it vanishes at the surface (among other desirable properties, see below). The 2d model captures the essential

[2] The gravitationally unstable discretization errors are not inherent to the parameterization, but to the paucity of the 2d model itself (little diffusivity and no gravity waves). Any realistic model with complete physics should not require convective adjustment.

[3] Seven days are required to reach finite amplitude in the 3d model because the initial perturbations are artificially small. In test simulations, and presumably also the ocean, larger initial perturbations develop into finite amplitude MLEs within one day. Thus MLE growth is fast enough to compete with other ML processes and wind changes, etc. (See also BFF).

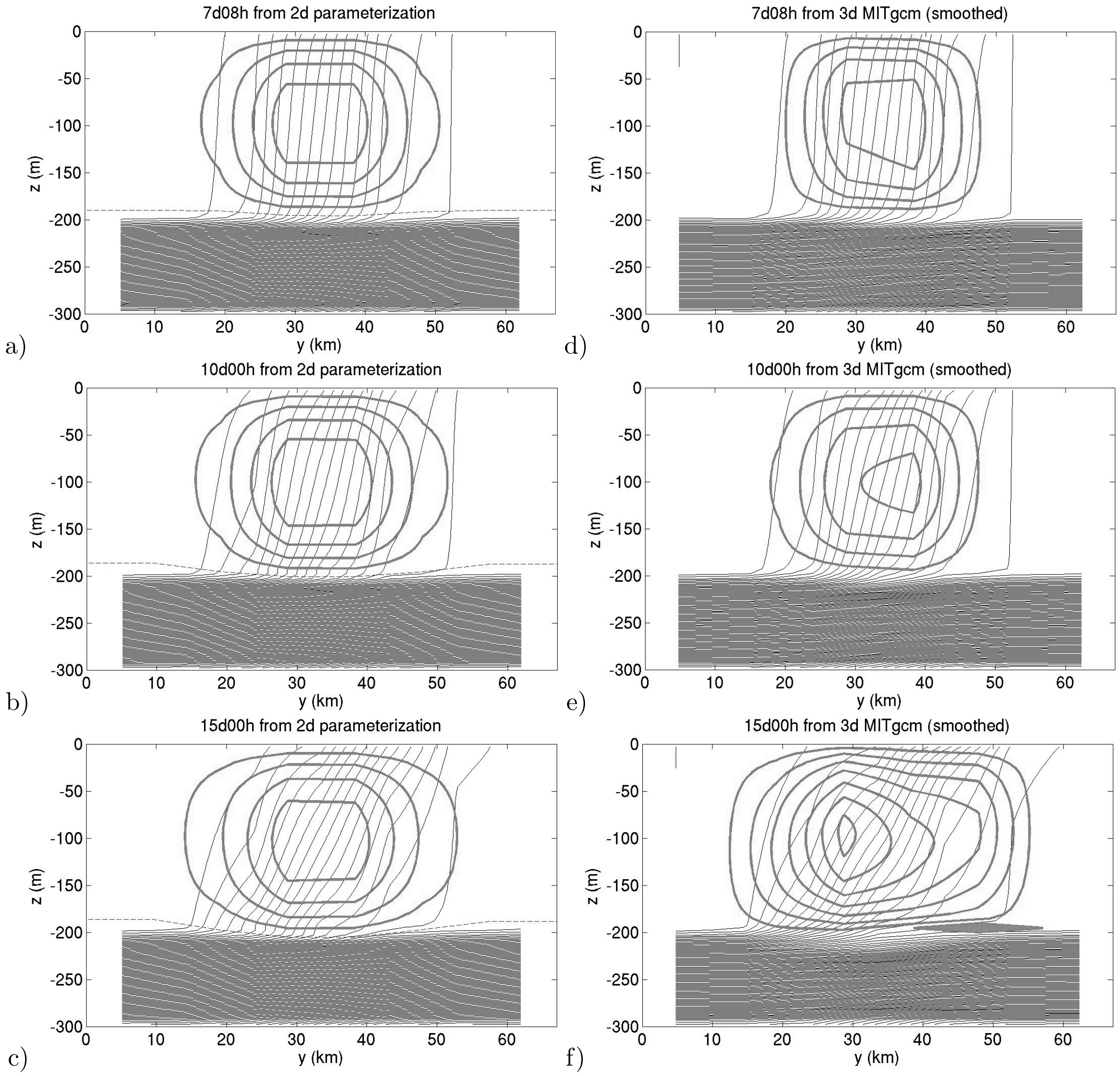

FIGURE 3: Streamfunction (Ψ_{hs}, thick) and smoothed buoyancy ($\bar{\bar{b}}$, thin) from (a-c) the 2d MLE parameterization at 9.6km resolution (dashed line shows diagnosed ML depth) and (d-f) the 3d MITgcm simulation at 450m resolution. The 2d model buoyancy is initialized from the 3d model $\bar{\bar{b}}$ at day 7. Variables from the 3d model are averaged onto the coarse 2d model grid, and contour intervals are the same in all figures. The timing of fig. 3d was selected to be a snapshot in the middle of an inertial oscillation of Ψ in the 3d model.

shape and magnitude of the streamfunction and reproduces the smoothed buoyancy of the 3d model remarkably well, even though it has a dimension fewer and twenty times coarser cross-channel resolution. Both in the 2d and the 3d simulation, the overturning is confined to the ML frontal region. FFH remark that the scaling used to convert extraction of potential energy to a local flux of buoyancy relies upon replacing a basin-wide average of $\overline{\overline{\overline{w'b'}}}$ with a local value in y. The strong agreement between the 3d and 2d models confirms this assumption. Testing other 3d simulations from FFH confirms that the agreement between the 2d and 3d models chosen here is typical.

The instantaneous streamfunctions do differ between the 3d and 2d models. If the 3d simulation is not smoothed to the coarser grid of the 2d model, smaller structures appear (Fig. 4). However, these cells are due to transient powerful MLEs that temporarily bias the along-channel averaging. Their

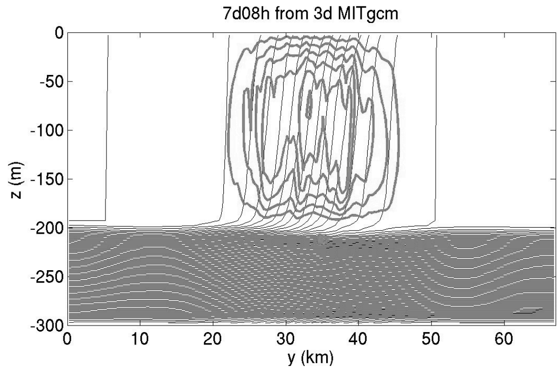

FIGURE 4: The equivalent to Fig. 3d without coarse grain averaging in y.

anomalous effect would vanish under sufficient ensemble averaging. Furthermore, the magnitude of the streamfunction is not matched exactly in any given snapshot, partly due to temporal fluctuations in the MLE statistics, and partly due to the presence of internal gravity waves. The latter add variability to snapshots of Ψ_{hs} but do not contribute irreversible restratification. The former are of negligible importance, because they do not affect the primary parameterization goal of representing the changes to buoyancy, which are a time-integrated–and thus smoothed–consequence of the streamfunction.

b. *Reproducing the Restratification*

The buoyancy fields in the 2d and 3d models are remarkably similar. The width of the front and the isopycnal slope are nearly indistinguishable for more than a week (Fig. 3). At later times boundary effects become important and the simulation is stopped because the sidewalls are an artifact of the numerical simulation. The primary purpose of the parameterization is to reproduce the restratification of strong baroclinic fronts, as explained in FFH. Restratification controls the depth to which subsequent mixing events will penetrate, and hence affects air-sea fluxes and surface to subsurface exchange. Fig. 5a shows that the average rate of restratification is well captured by the parameterization. Comparisons between 2d prognoses of other 3d model simulations indicates that discrepancies shown in Fig. 5a are typical: N^2 forecasts remain within a factor of 2 of the 3d model while the restratification covers up to two orders of magnitude increase in N^2.

FFH propose two different forms for the vertical structure of $\mathbf{\Psi}$ which differ in their accuracy. They are compared in Fig. 5b. The first, $\mu(z)$, is correct to second order in Rossby number and is quartic. The second, $\mu_2(z)$ is quadratic and correct only to first order in Rossby number,

$$\mu(z) = \left[1 - \left(\tfrac{2z}{H} + 1\right)^2\right]\left[1 + \tfrac{5}{21}\left(\tfrac{2z}{H} + 1\right)^2\right], \quad (9)$$

$$\mu_2(z) = \left[1 - \left(\tfrac{2z}{H} + 1\right)^2\right]. \quad (10)$$

A quadratic vertical structure is common to many eddy parameterizations (*e.g.,* Stone, 1972b; Canuto and Dubovikov, 2005). It is, after all, the simplest form that is symmetric about the ML center (as in simulations) and vanishes at the surface and ML base (trapping the overturning in the ML). It provides a nearly constant rate of restratification at all depths in the ML, as the eddy-induced velocity shear is constant ($\hat{\mathbf{z}} \times \mathbf{\Psi}_{zz}$). The resulting profiles of N^2 are nearly depth-independent (thin dashed lines in Fig. 5b). In contrast, restratification by the quartic form ($\mu(z)$) proceeds more quickly at the surface and ML base than in the interior–a behavior of the 3d model (Fig. 5b). Given the tiny additional cost of calculating $\mu(z)$ over $\mu_2(z)$, the former is recommended.

There are a few small discrepancies in the vertical structure of N^2 between the 2d and 3d models in Fig. 5b. First, N^2 is underestimated near the surface in the 2d model. The near-surface restratification in the 3d model is the result of frictional Ekman fluxes, generated by the no stress boundary condition at the surface, that drive light water over dense across the frontogenetic meanders (Fig 2). No attempt was made to reproduce this effect in the parameterization for two reasons. First, the addition of a diurnal cycle generates ample nighttime turbulence to overcome this restratification and substantially more solar daytime near-surface restratification. Second, much of this effect would already be present in a GCM with a full momentum equation.

A second discrepancy occurs near the base of the ML (Fig. 5b near -180m). There the 2d model again underpredicts restratification. The 2d model is particularly sensitive to the algorithm for determination of ML depth. As the ML restratifies the diagnosed ML depth becomes too shallow in this run of the 2d model, and restratification does not penetrate as deeply as the 3d model restratification. Increasing the vertical diffusivity from $10^{-5}\mathrm{m}^2/\mathrm{s}$ to $3{\cdot}10^{-5}\mathrm{m}^2/\mathrm{s}$ at all depths smooths out the base of the ML and allows the algorithm to work more robustly as shown in Fig. 5c. The value and physical significance of the diffusivity tested are discussed further in section 2c.

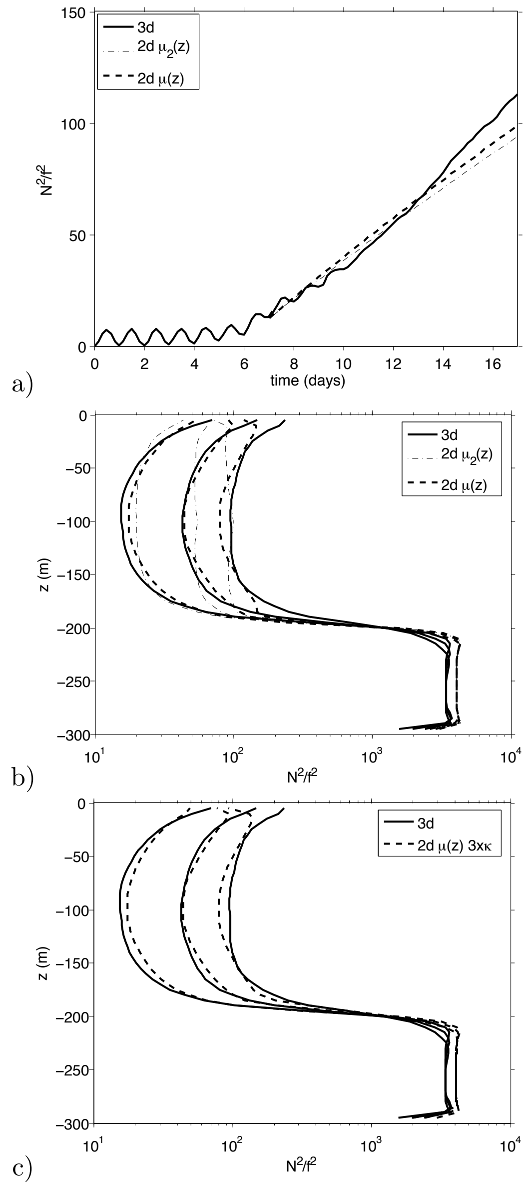

FIGURE 5: a) The vertical average of N^2 over $-175\text{m} < z < -25\text{m}$ and b) snapshots of N^2 from the 2d parameterization with two different vertical structure functions and the 3d simulation. c) is like b) but for a 2d model with $\kappa_v = 3 \cdot 10^{-5}\text{m}^2/\text{s}$, three times larger than in b).

c. *Reproducing the Eddy Fluxes*

The streamfunction in Fig. 3 from the 2d model agrees well with the 3d model $\Psi_{\rm hs} = \frac{\overline{\overline{w'b'}}}{\overline{\overline{b}}_y}$, and the restratification rate is well captured, so it is no surprise that the 2d $\Psi_{\rm hs}\overline{\overline{b}}_y$ and 3d $\overline{\overline{w'b'}}$ averaged over a three day window agrees to within 20% in the ML (Fig. 6a). The previous section demonstrated that the 2d model has substantial skill in predicting changes in $\overline{\overline{b}}$ in the 3d model, which reflects skill in predicting the average value of $\nabla \cdot \overline{\overline{\mathbf{u}'b'}}$ in the overall buoyancy equation (1). However, there are some discrepancies between the 2d and 3d models worth noting, not because they have substantial impact, but because they provide physical insight.

As noted in FFH, the vertical fluxes in the 3d model reverse sign slightly below the ML base (Fig. 6a near -210m). This overshoot is due to the continuity of w' in the face of discontinuity in isopycnal slope. FFH argue that this might be represented as a diffusivity, since it is a transport of buoyancy down the mean vertical gradient. In this particular simulation, it is equivalent to a κ_v near $3 \cdot 10^{-5}\text{m}^2/\text{s}$ just below the ML base. This diffusivity should change with parameters, just as $\overline{\overline{w'b'}}$ in the ML does. The added diffusivity to represent this flux gives physical motivation to the improvement in Fig. 5c over Fig. 5b. Fine tuning was not necessary for the MLE parameterization to improve in Fig. 5c: the added diffusivity applied in Fig. 5c was crudely applied throughout the water column and there is little sensitivity to the magnitude ($5 \cdot 10^{-5}\text{m}^2/\text{s}$ works similarly well). Enhancing κ_v only near the ML base provided similar improvement with negligible differences elsewhere. Of course, even the enhanced value of diffusivity is relatively low considering that the model is run for only a few days, so that only very sharp buoyancy features are notably diffused such as those near the ML base in Fig. 5b. It is well-known that ML parameterizations require parameterizations of turbulence penetrating below the ML base to reduce overly strong buoyancy jumps at the ML base. Typically, the diffusivities found here are sufficiently small to be overcome in a realistic model by a turbulence parameterization with penetrating mixing below the ML base (*e.g.,* Large et al., 1994). A more complete study of entrainment by MLEs would be interesting, particularly given the potential impacts on biology and chemical tracers, but is beyond the scope of the work here.

The magnitude of the horizontal fluxes in the 2d and 3d models disagree by approximately a factor of two (Fig. 6b). Most of the difference is the *residual* flux, $\mathbf{R}$, which is the diabatic part of the eddy fluxes that is not represented an overturning streamfunction,

$$\overline{\overline{\mathbf{u}'b'}} \equiv \mathbf{\Psi} \times \nabla\overline{\overline{b}} + \mathbf{R}. \tag{11}$$

In a statistically-steady, adiabatic flow, the fluxes would be along isopycnals, the skew flux ($\mathbf{\Psi} \times \nabla\overline{\overline{b}}$)

would capture the full flux, and $\mathbf{R}$ would be zero. However the time dependence here allows the fluxes to be partly across mean isopycnals to slump the front. Thus, the mean fluxes are not along mean isopycnals and $\mathbf{R}$ is nonzero (McDougall and McIntosh, 1996). The Held and Schneider (1999) definition of the overturning streamfunction, Ψ_{hs}, is used here because it makes reproducing the restratifying vertical flux and the surface boundary condition trivial,

$$\boldsymbol{\Psi}_{\mathrm{hs}} \equiv \frac{\nabla\bar{\bar{b}} \times \hat{\mathbf{z}}\ \overline{\overline{w'b'}}}{|\nabla\bar{\bar{b}}|^2}. \tag{12}$$

The definition (12) captures all of the vertical flux, and leaves an horizontal residual flux.

$$\overline{\overline{w'b'}}\hat{\mathbf{z}} = \boldsymbol{\Psi}_{\mathrm{hs}} \times \nabla_H \bar{\bar{b}}, \tag{13}$$

$$\overline{\overline{\mathbf{u}'_H b'}} = \boldsymbol{\Psi}_{\mathrm{hs}} \times \hat{\mathbf{z}}\bar{\bar{b}}_z + \mathbf{R}. \tag{14}$$

Fig. 6b shows that $\overline{\overline{\mathbf{u}'_H b'}}$ has roughly the same shape as $\boldsymbol{\Psi}_{\mathrm{hs}} \times \hat{\mathbf{z}}\bar{\bar{b}}_z$, so to a good approximation,

$$\overline{\overline{\mathbf{u}'_H b'}} \approx C\boldsymbol{\Psi}_{\mathrm{hs}} \times \hat{\mathbf{z}}\bar{\bar{b}}_z, \tag{15}$$

$$\mathbf{R} \approx (C-1)\boldsymbol{\Psi}_{\mathrm{hs}} \times \hat{\mathbf{z}}\bar{\bar{b}}_z. \tag{16}$$

The impact including $\mathbf{R}$ in the 2d model is studied using (16).

As an interesting side note, the constant of proportionality C is also the ratio of the isopycnal slope to the slope along which the eddy fluxes occur (see also FFH). Eady (1949) notes that $C = 2$ optimizes the extraction rate of PE. In the linear solution $C = 2$ only at the mid-depth. Fig. 6b shows that the finite-amplitude problem tends toward a constant value of C at all depths so that PE is extracted equally throughout the ML. The reason why the total, skew, and residual horizontal fluxes share the same vertical structure is thus physically motivated by energetic considerations. An important component of the tendency toward uniform C is the increased restratification near the ML edges. Recall that the 2d $\mu(z)$ model has this effect and the 2d $\mu_2(z)$ model does not. The former has $\overline{\overline{v'b'}}$ that resembles the 3d model more than the latter in Fig. 6b, so increased restratification and shallower isopycnal slopes near the ML edges are important in equal extraction of PE at all depths.

FFH argue that $\mathbf{R}$ may be safely neglected as it is smaller than the mesoscale horizontal fluxes. This view is supported by the agreement in the 2d and 3d model $\bar{\bar{b}}$ in the last section. Fig. 6c shows that $\bar{\bar{b}}_y$ changes only by 15% over ten days in the 3d model, as MLEs are primarily overturning rather than diffusing the front. Half of this decrease is captured without the residual flux, and merely changing the advection scheme affects $\bar{\bar{b}}_y$ to the same degree (Fig. 6c, dotted). While adding $\mathbf{R}$ from (16) explicitly makes up the additional half of the horizontal flux, it makes the model substantially less stable numerically (see Appendix A). Thus, the modest effects of MLE residual fluxes are outweighed by the costs of parameterizing them.

To summarize, a 2d coarse resolution prognostic model based on the parameterization proposed here does a surprisingly good job at reproducing the shape and magnitude of the eddy-induced overturning in a particular 3d simulation. The horizontal residual flux may be safely neglected, and adding some vertical diffusivity at the ML base improves the 2d model somewhat (which will occur naturally in a realistic model with turbulent transition layer parameterizations). Running the prognostic model side-by-side with other 3d simulations gives similar results: the 3d simulations are generally more variable in time and space than the parameterization, but the integrated effect is reproduced so that N^2 (and M^2) remain within a factor of two (within 20%) between the 2d parameterization and the 3d simulation while N^2 increases over two orders of magnitude.

3. Global Impact Estimate from Observations

The preceding section demonstrates that the MLE parameterization is effective, but it does not demonstrate any sensitivity of the climate system to the process being parameterized. This section demonstrates that the vertical fluxes (and associated restratification) obtained from the MLE parameterization will frequently play an O(1) role in the ML buoyancy budget, and hence in the interaction between the ocean and atmosphere.

Satellite observations and ML depth climatologies are used to infer the regions where MLEs might be expected to drive large vertical fluxes. The goal is to estimate the equivalent vertical heat flux due to

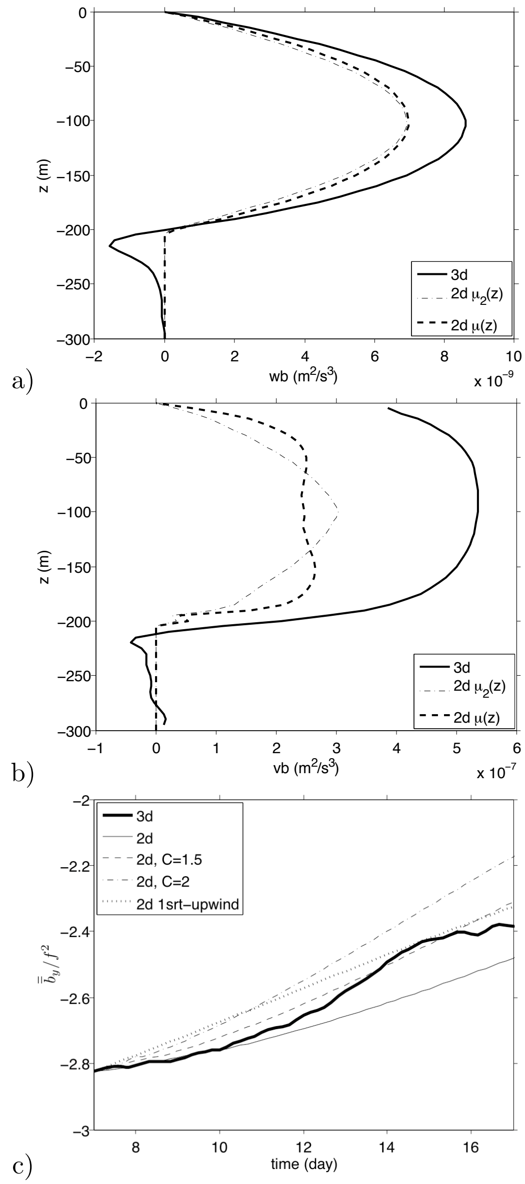

FIGURE 6: MLE fluxes a) $\overline{\overline{w'b'}}$ and b) $\overline{\overline{v'b'}}$ from the 2d and 3d models (averaged from day 10.5 to 13.5). The 2d skew fluxes , $\boldsymbol{\Psi} \times \nabla\overline{\overline{\mathbf{b}}}$, attempt to reproduce the 3d fluxes by (2) and are shown. The advective fluxes, $\overline{\overline{b}}\nabla \times \boldsymbol{\Psi}$, differ greatly other than in flux divergence, see (22). c) Comparison of $\overline{\overline{b}}_y/f^2$ from the 3d run and 2d runs with different parameterizations of the residual flux. All variables averaged over 20km in y centered on the front.

MLE restratification using the parameterization (3),

$$
\begin{aligned}
c_p\rho\overline{\overline{w'T'}} &= \frac{c_p\rho}{g\alpha_T}\overline{\overline{w'b'}} \\
&= \frac{c_p\rho}{g\alpha_T}\boldsymbol{\Psi} \times \nabla_H\overline{\overline{b}}^z \\
&= \frac{c_p\rho}{g\alpha_T}\frac{C_e\left|\nabla\overline{\overline{b}}^z\right|^2 H^2}{|f|}. \qquad (17)
\end{aligned}
$$

MLE fluxes are a rearrangement of buoyancy and not a source, but converting to heat flux units allows ready comparison of the MLE restratifying fluxes to air-sea heat fluxes.

The temperature-based ML depth climatologies of de Boyer Montégut et al. (2004) and a density-based ML depth based on Levitus and Boyer (1994) are used to estimate H in (17). The former is more accurate as ML depth is estimated from individual hydrographic profiles. However, it is based on temperature profiles rather than density in order to provide global coverage. For example, de Boyer Montégut et al. (2004) note that their ML depth estimate is too shallow north of 60° latitude, so the estimate from (17) may be even an order of magnitude too small there. They also note poor results in equatorial regions due to rainfall, but equatorial data are not used here. Levitus provides a density-based definition of ML depth, but temperature and salinity are spatially-averaged before calculating ML depth. The resulting uncertainty is believed to be even larger than the bias introduced by using only temperature to determine ML depth. For present purposes, the climatologies are similar enough to ensure estimates of (17) agree within a factor of four in most regions. For subsequent results, de Boyer Montégut et al. (2004) is used.

The horizontal buoyancy gradient is more difficult to determine. Using a climatology, such as Levitus, vastly underestimates mesoscale gradients due to smoothing. Using satellite sea surface temperature overestimates the relevant buoyancy gradients. Attempts were made with a number of satellite-based SST products, but all produced vertical fluxes from (17) so large that they dominated surface fluxes throughout the global ocean and would rapidly restratify the ML worldwide. If the temperature gradients observed resulted in buoyancy gradients they would immediately yield to instabilities and slump down. The observational evidence that these small-scale temperature gradients persist is an indication of unobserved compensating salinity gradients (Rudnick and Ferrari, 1999; Hosegood et al., 2006).

Alternatively, satellite altimetry can be used to provide a sufficiently accurate estimate of $|\nabla\overline{\overline{b}}|$. Stammer (1998) provides a map of EKE $= (u^2 + v^2)/2$ over the extratropical oceans inferred from satellite altimetry. This kinetic energy can be developed into an estimate of ML horizontal buoyancy gradients by the following method. First, the velocity shear is assumed to be in thermal wind balance,

$$|\nabla\bar{\bar{b}}|^2 = f^2 \left|\frac{\partial \bar{\bar{\mathbf{u}}}_H}{\partial z}\right|^2 = 2f^2 \mathrm{EKE} \frac{\left|\frac{\partial \bar{\bar{\mathbf{u}}}_H}{\partial z}\right|^2}{\left|\bar{\bar{\mathbf{u}}}_H\right|^2}. \tag{18}$$

Wunsch (1997) shows that the majority of the energy observed by altimeters is first mode baroclinic. If the vertical shear of the velocity is assumed to be first-mode baroclinic, then the buoyancy gradient estimate can be written in terms of a decay scale for that mode, H_t,

$$|\nabla b|^2 \quad = \quad 2f^2 \mathrm{EKE} \frac{1}{H_t^2}. \tag{19}$$

Appendix B gives the method for estimating H_t (based on a WKBJ approximation for the first baroclinic mode based on Levitus climatology), but simply using 1km everywhere yields similar results. Since altimetry provides roughly 1/4 degree resolution, energy at roughly the first baroclinic mode deformation radius is captured in most places providing a lower estimate on mesoscale buoyancy gradients.

Thus, the estimation for the scaling (17) is

$$c_p \rho \overline{\overline{w'T'}} \quad = \quad \frac{c_p \rho}{g \alpha_T} 2C_e |f| \mathrm{EKE} \frac{H^2}{H_t^2}. \tag{20}$$

All remaining parameters in (20) are well known and appear in Table 3. The region near the equator is blocked out, because the Stammer (1998) dataset and equation (20) are not valid there.

Symbol	Name	Value
g	gravitational accel.	9.81 m s^{-2}
c_p	specific heat	4180 J kg^{-1}K^{-1}
ρ	typical density	1025 kg m^{-3}
α_T	thermal exp. coeff.	$2 \cdot 10^{-4}$ K^{-1}
C_e	stirring eff. coeff.	0.06
$\|f\|$	Coriolis parameter	$1.45 \cdot 10^{-4}$ s^{-1} $\times\|\sin(latitude)\|$

TABLE 3: Constants used for the flux estimation in (20).

The two panels of Fig. 7 show the estimated MLE vertical flux from (20) for austral and boreal wintertime conditions. The most obvious features are strong signals where the ML is deep. That is, the North Atlantic and Pacific in boreal winter and the Southern Ocean in austral winter. Some contribution stems from the distribution of the horizontal buoyancy gradients as well (these regions also have strong mesoscale activity). However, mesoscale activity is relatively consistent year-round (Qiu, 1999; Qiu and Chen, 2004), while the ML depths vary strongly. The most active areas are those where active convection is occuring. Where surface cooling is large, such as mode water and deep water formation regions, the MLEs are predicted to restratify the regions after convection. Because these regions are crucial for communication between the atmosphere and ocean, neglecting the MLE fluxes may be a significant bias.

MLE fluxes are often comparable to the air-sea fluxes: they are large where air-sea fluxes are large (Fig. 7), and even where they are weaker in Fig. 7 the air-sea fluxes are comparably weaker. Comparing to the Grist and Josey (2003) heat flux dataset, the MLE heat flux estimate exceeds 50% of the climatological monthly-mean heat flux more than 25% of the time and exceeds 5% of the climatological flux more than 50% of the time. Of course, the MLE fluxes are overwhelmed during active convection events in times of extreme heat fluxes, but their fluxes are comparable to the monthly mean fluxes and will restratify after cooling events.

The restratification by frontogenesis (Oschlies, 2002; Lapeyre et al., 2006; Capet et al., 2006) may be of similar magnitude to MLE restratification. However, the simulation in FFH including mesoscale eddies and submesoscale MLEs indicates that frontogenetic restratification will be added to rather than instead of MLE restratification. The MLE parameterization applies even when mesoscale frontogenesis is resolved. A second restratification process of recently studied is wind-driven restratification (Thomas and Lee, 2005). The winds may drive ageostrophic circulations of comparable magnitude to MLE-induced overturning. However, depending on the direction of the wind, these effects may be destratifying or restratifying. The net effect of a random wind field remains unclear. An added complication is that wind-driven ageostrophic circulations can tighten fronts and promote the development of MLEs, hence coupling the two processes (L. Thomas, personal communication). Ferrari and Thomas (2007) find that MLEs are often at leading order. Wind effects and mesoscale frontogenesis are also important, but any future parameterizations of these effects can be added to or used to improve the MLE parameterization here. In sum, it seems the effects of MLEs will be felt often throughout the extratropical ML.

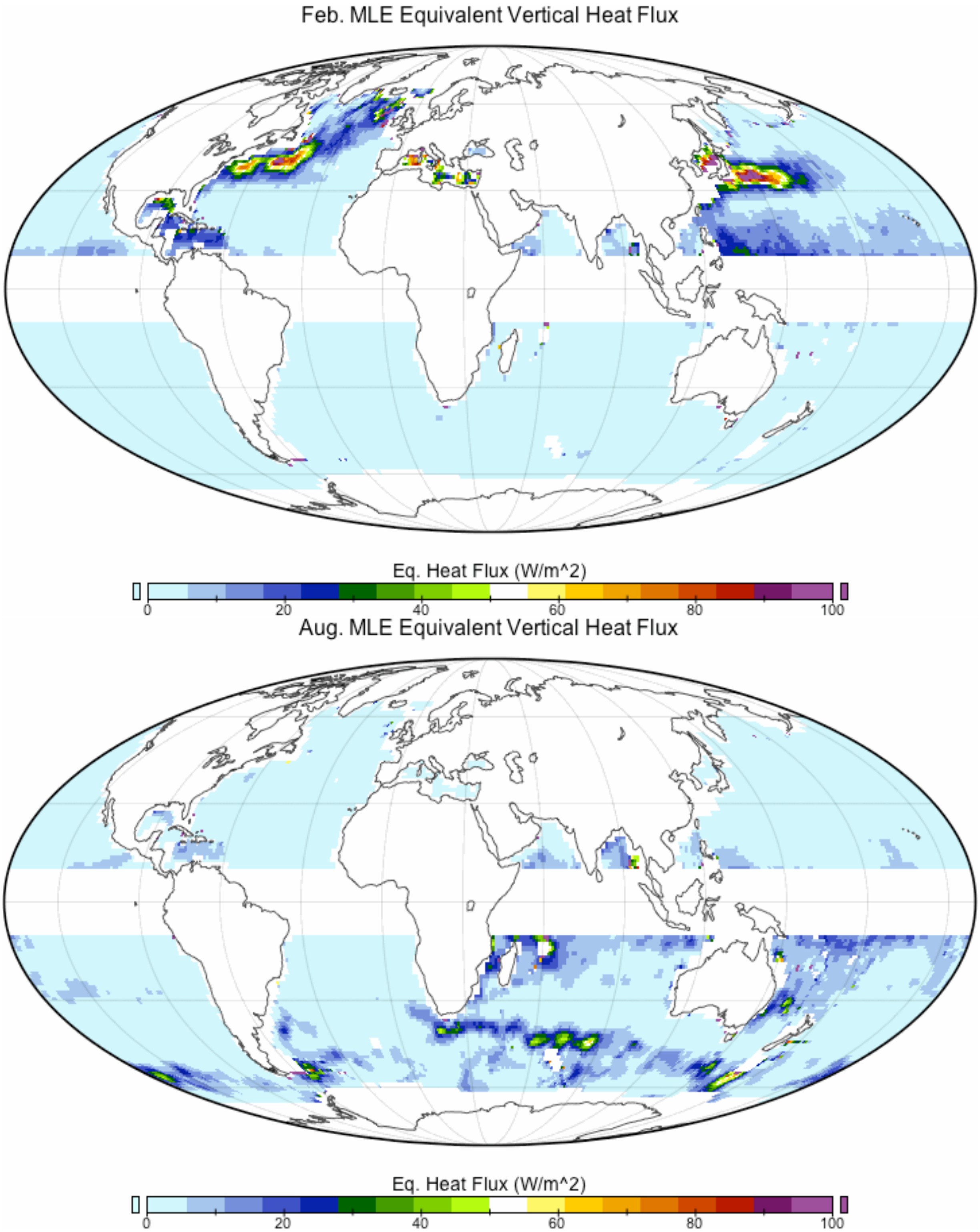

FIGURE 7: Equivalent vertical heat flux due to submesoscale restratification of the ML inferred from satellite altimetry (Stammer, 1998), the and the de Boyer Montégut et al. (2004) mixed layer depth climatology.

4. Summary and Conclusion

This paper has demonstrated that the parameterization proposed in Fox-Kemper et al. (2007a) is effective at reproducing idealized submesoscale resolving simulations. The implied vertical heat fluxes were estimated from observations and found to be a leading order contribution to the mixed layer buoyancy budget. Mixed layer eddies are effective at restratifying the mixed layer throughout the world, and will have an important effect where atmosphere-ocean coupling is important. MLE restratification is presently ignored in most ocean studies and in all coarse resolution models.

The parameterization proposed by FFH takes the form of an overturning streamfunction depending on the horizontal buoyancy gradients, which is not true of any other parameterizations commonly used for ML processes. Thus, this parameterization will provide GCMs with a novel ML depth and buoyancy sensitivity. The implementation of the parameterization here confirms that the overturning streamfunction captures the change in the buoyancy in these simulations remarkably well, and that it is readily and stably implemented with many different advection schemes.

Simulations of the spindown of initial fronts by eddies like this one, which is a situation relevant in some ocean conditions, are far fewer than equilibrated simulations, which are obviously appropriate for the atmosphere where radiative cooling is critical (*e.g.,* Held and Suarez, 1994). In fact, spindown simulations are so uncommon that the authors were suprised to find that a sensible parameterization could be found. The tendency toward equal extraction of PE at all depths, as demonstrated by Fig. 6b, is a purely finite-amplitude effect and is potentially significant for all spindown problems, including spindown of large-scale ocean fronts by mesoscale eddies. However, the complications of variable N^2 and potential vorticity in the mesoscale eddy problem are nontrivial. Nonetheless, equal extraction would imply a strong departure for spindown problems from the exactly along-isopycnal fluxes deemed appropriate for spindown by Gent and McWilliams (1990), and is yet to be fully tested for problem of spindown by mesoscale eddies.

The parameterization as tested here may be applied directly in mesoscale eddy-resolving models of the extratropics. However, it must be adapted on the equator (because of division by $|f|$) and can not be included in coarse horizontal resolution ocean models (because they will underestimate the relevant $\nabla_H \bar{\bar{b}}$). These remaining difficulties are addressed in Fox-Kemper et al. (2007b), where the effects of the parameterization are studied both in a realistic eddy-resolving model of the Southern Ocean and a 1° global coupled atmosphere-ocean model.

Ensemble averages of the 3d simulations would allow a closer critique of the flaws in the details of the prognostic model, but since the parameterization is intended to be used in coarser-resolution models where such differences will be subgridscale, this extra step seems unnecessary. To the extent that the frontal spindown simulation is an adequate prototype for the real MLEs in the ocean, the parameterization has remarkable skill. Additional effects to be considered in the future include the effect of winds and coupling with the mesoscale. Of course, the ocean is not as simple as the idealized situation considered here, nonetheless the results here are very encouraging and the approximate effects of mixed layer eddies may now be explored with ease in many models.

Acknowledgement This work was supported by NSF grant OCE-0612143. Discussions with G. Flierl, R. Hallberg, W. Large, L. Thomas, and J. Marshall contributed greatly to this work. Group discussions with the CPT-EMILIE team also contributed.

A. 2d Prognostic Model Details

The prognostic models uses $\mathbf{\Psi}$ from (3) to advect buoyancy, implemented with a staggered grid finite-volume method identical to that used in the 3d model (Marshall et al., 1997) where temperature gridcells are surrounded by fluxes through the cell faces in y and z. The solution method begins with a $\bar{\bar{b}}$ field discretized to cell centers, uses (3) to determine $\mathbf{\Psi}$ (located on cell corners), then differentiates $\mathbf{\Psi}$ to generate eddy-induced velocities v^*, w^* as in (6), and the buoyancy is evolved as in (5). Different buoyancy advection schemes are used to appropriately form $\overline{\overline{v'b'}}$ and $\overline{\overline{w'b'}}$ from v^*, w^* and $\bar{\bar{b}}$. First-order upwind, Lax-Wendroff, 3rd-order upwind with and without flux limiters, and explicit diffusivity with second and fourth order centered schemes yield similar results, with expected minor differences in the degree of gridscale noise. No obvious numerical instabilities occurred in any scheme. A third order upwind, flux-limited scheme is used throughout, except where specifically mentioned. Convective adjustment is used to eliminate occasional unstable stratification due to discretization errors and mistaken determinations of ML base location. Timestepping is done by an fifth-order Runge-Kutta method with an embedded fourth-order method to set time steps adaptively. The timesteps allowed at $< 0.1\%$ accuracy were quite long (8hr), so the CFL condition on the overturning should not be troublesome in implementation in a GCM.

The ML depth H is determined by the integral constraint,

$$N^2(H) - \min(N^2) = \frac{C_m}{H}\int_{-H}^{0}(N^2(z'))\mathrm{d}z', \quad (21)$$

Where here $C_m = 8$. The minimum ML value of N^2, $\min(N^2)$, in the ML is a very small correction to the l.h.s., but allows a larger (and thus more robust) value of C_m to be used than was used in FFH. Nonetheless subtracting it from the local value of N^2 reduced the number of spurious ML depths that occured when N^2 happened to vary within the ML.

The residual fluxes are added in Section 2c. They are determined by noting that the 3d horizontal flux has a similar shape to the 2d horizontal skew flux in Fig. 5b, so to a good approximation,

$$\overline{\overline{\mathbf{u}'_H b'}} \approx C\mathbf{\Psi}_{\mathrm{hs}} \times \hat{\mathbf{z}}\overline{\overline{b}}_z,$$
$$\mathbf{R} \approx (C-1)\mathbf{\Psi}_{\mathrm{hs}} \times \hat{\mathbf{z}}\overline{\overline{b}}_z.$$

The latter allows direct estimation of the residual flux.

Calculating the residual flux requires an additional step beyond the standard approach to advection taken here. Typically, the advection of buoyancy is calculated as advective-form fluxes $(v^*, w^*)\overline{\overline{b}}$, which are calculated as $\overline{\overline{b}}(\nabla \times \mathbf{\Psi})$ with upwinding and flux limiting for stability taken into account. The following identity asserts that the divergence of the advective fluxes ($(v^*, w^*)\overline{\overline{b}} \equiv \left[\overline{\overline{b}}(\nabla \times \mathbf{\Psi})\right]$) will equal the divergence of the skew fluxes ($\mathbf{\Psi} \times \nabla\overline{\overline{b}}$),

$$\begin{aligned} 0 &= \nabla \cdot (\nabla \times \mathbf{\Psi}\overline{\overline{b}}), \\ &\equiv \nabla \cdot \left[\overline{\overline{b}}(\nabla \times \mathbf{\Psi})\right] - \nabla \cdot \left[\mathbf{\Psi} \times \nabla\overline{\overline{b}}\right]. \end{aligned} \quad (22)$$

The discretization assures that this identity holds to machine precision. Since only divergences affect the buoyancy budget, (5), this identity is sufficient to ensure that the buoyancy evolution and numerical stability is identical whether advective or skew fluxes are used to transport buoyancy.

In (16), it was argued that the residual flux is roughly proportional to the skew flux, which must be determined. The model advects buoyancy with the advective flux after upwinding for stability. The skew flux can be calculated from the already upwinded advective flux with,

$$\nabla \times \left(\mathbf{\Psi}\overline{\overline{b}}\right) + \mathbf{\Psi} \times \nabla\overline{\overline{b}} = \overline{\overline{b}}(\nabla \times \mathbf{\Psi}).$$

The residual flux is then just $(C-1)\mathbf{\Psi} \times \nabla\overline{\overline{b}}$. The residual flux gains some of the upwinding and flux-limiting that are endowed on the horizontal skew flux by upwinding the horizontal advective flux before transforming to the skew form. However, the residual flux cannot be further upwinded or flux limited after this transformation. The horizontal skew and residual fluxes are a product of a streamfunction (very smooth) times a buoyancy gradient (very noisy) which is a much less stable arrangement than a product of velocity (somewhat smooth) and buoyancy (somewhat smooth). The only reason that a discretization based on the skew flux is stable here is the exact identity with the advective flux in (22) that was stabilized by upwinding. Once the residual flux is added, the identity is broken, and the skew plus residual does not correspond to an exact advective form.

The test cases in Fig. 6c are stabilized with much smaller time steps to allow the advection scheme's implicit diffusivity to exert stability. In a realistic ocean model, one could not afford smaller timesteps, so horizontal diffusivity would have to be increased to stabilize the residual flux, which amounts to double-counting the diffusive effects of MLEs! Fig. 6c shows that changing to a more diffusive advection scheme (in that case a first-order upwind scheme instead of a third order scheme) produces the same magnitude of changes as adding the residual flux, but *very* stably. Similarly, the residual flux could be implemented as a spatially and temporally variable nonlinear diffusivity as suggested in FFH, but spatially-variable diffusivities have their own numerical implementation difficulties (*e.g.,* Fox-Kemper and Pedlosky, 2004). In sum, the difficulties in implementing the residual flux outweigh the modest benefit in this problem, but if one insists on doing so using a first-order upwind advection scheme seems to be a practical approximation.

B. Determining H_t

The connection between the satellite altimetry and horizontal buoyancy gradients requires an estimate of the vertical decay scale of the first baroclinic mode, H_t. Following (Chelton et al., 1998), separation of variables is applied to find vertical mode solutions of the linearized quasigeostrophic potential vorticity equation. The resulting eigenvalue problem for the vertical velocity, $w = \phi(z)W(x, y, t)$, is of particular importance here,

$$\frac{d^2\phi(z)}{dz^2} = -\frac{N^2(z)}{c_1^2}\phi(z), \tag{23}$$

$$\phi = 0 \quad \text{at} \quad z = 0, \tag{24}$$

$$\phi = 0 \quad \text{at} \quad z = -D, \tag{25}$$

where D is the ocean depth. The assumption of separability, $w = \phi(z)W(x, y, t)$ and incompressibility, $\frac{\partial w}{\partial z} = -\nabla \cdot \mathbf{u}_H$, require that $\mathbf{u}_H$ has the vertical structure of $\frac{\partial \phi(z)}{\partial z}$. Thus, an estimate of H_t is,

$$\frac{1}{H_t^2} = \frac{\left|\frac{\partial \overline{\overline{\mathbf{u}}}_H}{\partial z}\right|^2}{\left|\overline{\overline{\mathbf{u}}}_H\right|^2} = \frac{\left|\frac{d^2\phi}{dz^2}\right|^2}{\left|\frac{d\phi}{dz}\right|}. \tag{26}$$

To the accuracy required here, the approximate WKB solution provided by Chelton et al. (1998) suffices,

$$\phi(z) = \sqrt{\frac{N(z)}{\int_{-D}^{0} N(z')\mathrm{d}z'}} B \sin\left(\frac{\int_{-D}^{z} N(z')\mathrm{d}z'}{\int_{-D}^{0} N(z')\mathrm{d}z'}\right). \tag{27}$$

Plugging the expression (27) for $\phi(z)$ into (26) and evaluating at z just below the ML depth gives a sufficiently accurate approximation to H_t for these purposes. The entire expression was evaluated globally using the Levitus climatology to produce a global map of H_t. Simply using $H_t = 1$km everywhere yields comparable, although less accurate, estimates than those produced with H_t estimated by this method.

REFERENCES

Boccaletti, G., R. Ferrari, and B. Fox-Kemper: 2007, Mixed layer instabilities and restratification. *J. Phys. Oceanogr.*, **35**, 1263–1278.

Canuto, V. M. and M. S. Dubovikov: 2005, Modeling mesoscale eddies. *Ocean Modeling*, **8**, 1–30.

Capet, X., J. McWilliams, M. J. Molemaker, and A. Shchepetkin: 2006, The transition from mesoscale to submesoscale in the california current system. *J. Phys. Oceanogr.*, submitted.

Chelton, D. B., R. A. Deszoeke, and M. G. Schlax: 1998, Geographical variability of the first baroclinic Rossby radius of deformation. *J. Phys. Oceanogr.*, **28**, 433–460.

de Boyer Montégut, C., G. Madec, A. S. Fischer, A. Lazar, and D. Iudicone: 2004, Mixed layer depth over the global ocean: An examination of profile data and a profile-based climatology. *J. Geophys. Res.*, **109**, C12003, doi:10.1029/2004JC002378.

Eady, E. T.: 1949, Long waves and cyclone waves. *Tellus*, **1**, 33–52.

Ferrari, R. and L. Thomas: 2007, Friction, frontogenesis, frontal instabilities and the stratification of the surface mixed layer. *J. Phys. Oceanogr.*, submitted.

Fox-Kemper, B., R. Ferrari, and R. W. Hallberg: 2007a, Parameterization of mixed layer eddies. I: Theory and diagnosis. *J. Phys. Oceanogr.*, submitted.

Fox-Kemper, B., R. W. Hallberg, and R. Ferrari: 2007b, Parameterization of mixed layer eddies. III: Global implementation and model impact. *J. Phys. Oceanogr.*, in preparation.

Fox-Kemper, B. and J. Pedlosky: 2004, Wind-driven barotropic gyre I: Circulation control by eddy vorticity fluxes to a region of enhanced removal. *J. Mar. Res.*, **62**, 169–193.

Gent, P. R. and J. C. McWilliams: 1990, Isopycnal mixing in ocean circulation models. *J. Phys. Oceanogr.*, **20**, 150–155.

Grist, J. P. and S. A. Josey: 2003, Inverse analysis adjustment of the soc airsea flux climatology using ocean heat transport constraints. *J. Climate*, **16**, 3274–3295.

Held, I. M. and T. Schneider: 1999, The surface branch of the zonally averaged mass transport circulation in the troposphere. *J. Atmos. Sci.*, **56**, 1688–1697.

Held, I. M. and M. J. Suarez: 1994, A proposal for the intercomparison of the dynamical cores of atmospheric general circulation models. *Bull. Am. Meteorol. Soc.*, **75**, 1825–1830.

Hosegood, P., M. Gregg, and M. Alford: 2006, Sub-mesoscale lateral density structure in the oceanic surface mixed layer. *Geophys. Res. Lett.*, submitted.

Lapeyre, G., P. Klein, and B. L. Hua: 2006, Oceanic restratification forced by surface frontogenesis. *J. Phys. Oceanogr.*, **36**, 1577–1590.

Large, W. G., J. C. McWilliams, and S. C. Doney: 1994, Oceanic vertical mixing: A review and a model with a vertical k-profile boundary layer parameterization. *Rev. Geophys.*, 363–403.

Levitus, S. and T. P. Boyer: 1994, World ocean atlas 1994 volume 4: Temperature. Technical Report 117pp, NOAA Atlas NESDIS 4, U.S. Department of Commerce, Washington, D.C.
URL `http://iridl.ldeo.columbia.edu/SOURCES/.LEVITUS94/`

Marshall, J. C., A. Adcroft, C. Hill, L. Perelman, and C. Heisey: 1997, A finite-volume, incompressible Navier-Stokes model for studies of the ocean on parallel computers. *J. Geophys. Res.*, **102**, 5753–5766.

McDougall, T. J. and P. C. McIntosh: 1996, The temporal-residual mean velocity. Part I: Derivation and the scalar conservation equations. *J. Phys. Oceanogr.*, **26**, 2653–2665.

Oschlies, A.: 2002, Improved representation of upper-ocean dynamics and mixed layer depths in a model of the north atlantic on switching from eddy-permitting to eddy-resolving grid resolution. *J. Phys. Oceanogr.*, **32**, 2277–2298.

Qiu, B.: 1999, Seasonal eddy field modulation of the North Pacific Subtropical Countercurrent: TOPEX/POSEIDON observations and theory. *J. Phys. Oceanogr.*, **29**, 2417–2468.

Qiu, B. and S. Chen: 2004, Seasonal modulations in the eddy field of the South Pacific Ocean. *J. Phys. Oceanogr.*, **34**, 1515–1527.

Rudnick, D. L. and R. Ferrari: 1999, Compensation of horizontal temperature and salinity gradients in the ocean mixed layer. *Science*, **283**, 526–529.

Stammer, D.: 1998, On eddy characteristics, eddy transports, and mean flow properties. *J. Phys. Oceanogr.*, **28**, 727–739.

Stone, P. H.: 1972a, On non-geostrophic baroclinic stability: Part III. The momentum and heat transports. *J. Atmos. Sci.*, **29**, 419–426.

— 1972b, A simplified radiative-dynamical model for the static stability of rotating atmospheres. *J. Atmos. Sci.*, **29**, 405–418.

Tandon, A. and C. Garrett: 1995, Geostrophic adjustment and restratification of a mixed layer with horizontal gradients above a stratified layer. *J. Phys. Oceanogr.*, **25**, 2229–2241.

Thomas, L. N. and C. M. Lee: 2005, Intensification of ocean fronts by down-front winds. *J. Phys. Oceanogr.*, **35**, 1086–1102.

Wunsch, C.: 1997, The vertical partition of oceanic horizontal kinetic energy. *J. Phys. Oceanogr.*, **27**, 1770–1794.